Microlensing as a possible probe of event-horizon structure in quasars

Tomozeiu, Mihai ; Mohammed, Irshad ; Rabold, Manuel ; Saha, Prasenjit ; Wambsganss, Joachim

DOI: https://doi.org/10.1093/mnras/stx3166

Monthly Notices
of the
ROYAL ASTRONOMICAL SOCIETY

MNRAS **475,** 1925–1936 (2018)
Advance Access publication 2017 December 8

doi:10.1093/mnras/stx3166

Microlensing as a possible probe of event-horizon structure in quasars

Mihai Tomozeiu,[1,2] Irshad Mohammed,[1,2,3] Manuel Rabold,[1,2] Prasenjit Saha[1,2]★ and Joachim Wambsganss[1,4]

[1]*Physik-Institut, University of Zurich, Winterthurerstrasse 190, CH-8057 Zurich, Switzerland*
[2]*Institute for Computational Science, University of Zurich, Winterthurerstrasse 190, CH-8057 Zurich, Switzerland*
[3]*Theoretical Astrophysics Group, Fermi National Accelerator Laboratory, Batavia, IL 60510, USA*
[4]*Zentrum für Astronomie der Universität Heidelberg, Mönchhofstrasse 12–14, D-69120 Heidelberg, Germany*

Accepted 2017 December 5. Received 2017 December 4; in original form 2016 April 5

ABSTRACT

In quasars which are lensed by galaxies, the point-like images sometimes show sharp and uncorrelated brightness variations (microlensing). These brightness changes are associated with the innermost region of the quasar passing through a complicated pattern of caustics produced by the stars in the lensing galaxy. In this paper, we study whether the universal properties of optical caustics could enable extraction of shape information about the central engine of quasars. We present a toy model with a crescent-shaped source crossing a fold caustic. The silhouette of a black hole over an accretion disc tends to produce roughly crescent sources. When a crescent-shaped source crosses a fold caustic, the resulting light curve is noticeably different from the case of a circular luminosity profile or Gaussian source. With good enough monitoring data, the crescent parameters, apart from one degeneracy, can be recovered.

Key words: gravitational lensing: micro – methods: numerical.

1 THE GENERAL PICTURE

Active galactic nuclei are thought to be powered by the accretion of matter from the proximal environment into a supermassive black hole. The radiation emitted excites the surrounding medium which becomes detectable as narrow line regions, broad line regions, and optical continuum. In the direction perpendicular to the accretion disc, where the medium is more transparent, the outflowing material tends to be collimated to jets. If the orientation is such that the observer's view of the central region is not blocked by the accretion disc or by a jet, a quasar is seen (e.g. Begelman, Blandford & Rees 1984). While the basic mechanism (originating in the work of Salpeter 1964; Zel'dovich & Novikov 1964; Lynden-Bell 1969) is not in doubt, the central engines, near the event horizons of the black holes, remain to be probed.

Modestly AGN are present in the Galactic Centre and in M87. In these two cases, the central engines (<0.1 mas on the sky) are close to being resolved through very long baseline interferometry, which shows preliminary indications of the jet-launching structures (Doeleman 2008; Doeleman et al. 2012; Fish et al. 2016). Current data do not deliver images but require fitting to predefined models for the images. A whole range of models have been applied, starting from simple geometric models to more complex physical models (Doeleman et al. 2008; Mościbrodzka et al. 2009; Dexter et al. 2010; Broderick et al. 2011). The more complicated models none the less tend to predict a crescent-shaped silhouette of the black hole. This motivated Kamruddin & Dexter (2013) to use a simple geometric crescent model to fit the available sub-mm interferometric data. They argued that the crescent is nothing but the silhouette of the event horizon. The great majority of quasars, however, lie at redshifts beyond 2 (Pâris et al. 2014) and their central engines would be orders of magnitude smaller on the sky. The direct observations of the black hole silhouettes of quasars are far beyond foreseeable instrumentation.

In the present paper, we consider a possible indirect method, related to Agol & Krolik (1999) and Mediavilla et al. (2015), through which gravitational microlensing could probe the black hole shadow and its proximal quasar environment.

Gravitational microlensing of quasars, reviewed in Section 2 below, is a phenomenon seen in quasars that have been multiply imaged by galaxies. Individual images in a multiple-image system can undergo sharp and seemingly random brightness changes. This can occur, even for constant intrinsic luminosity, as a consequence of two things: the very small size of the central engine, and granularity of the mass distribution of a lensing galaxy due to stars. The latter means that the local magnification is not a smooth function of source position. It contains a complicated network of singular curves, known as caustics. Fig. 1 shows part of a magnification map with a few caustics. The lensed brightness would be given by placing the source on such a magnification map and integrating the surface brightness weighted by the magnification. Most

★ E-mail: psaha@physik.uzh.ch

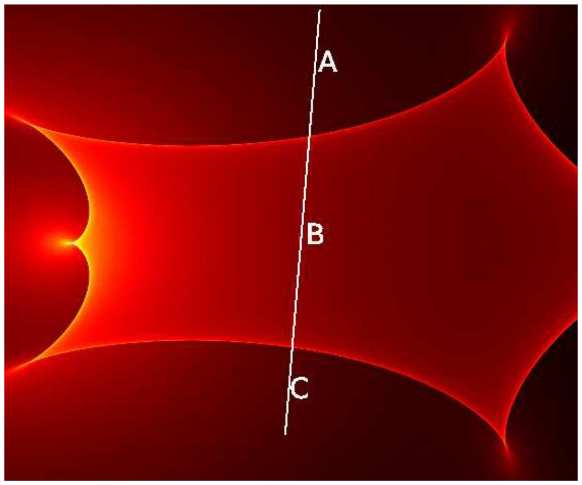

Figure 1. Magnification map used later in this paper (Section 5). The white line marks the trajectory of the centre of the sources for which the light curves presented in Figs 10–12 are generated. Note that this represents an atypically simple region of any realistic magnification map.

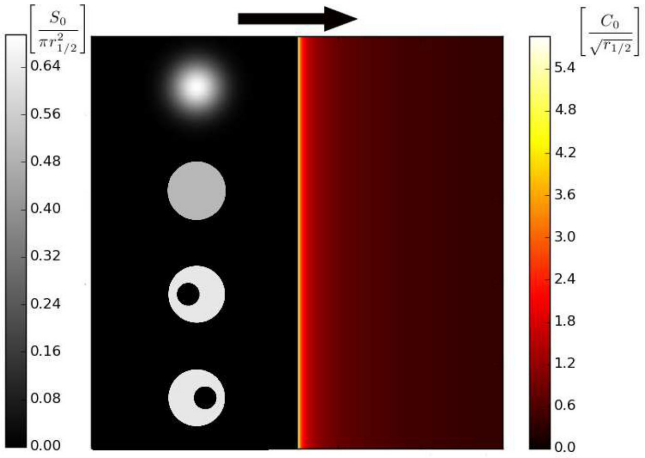

Figure 2. Source profiles for Gaussian, disc, crescents (right) and magnification map for an infinite fold (left). Objects have the same S_0 and $r_{1/2}$. The black arrow marks the direction of motion of the sources relative to the caustic.

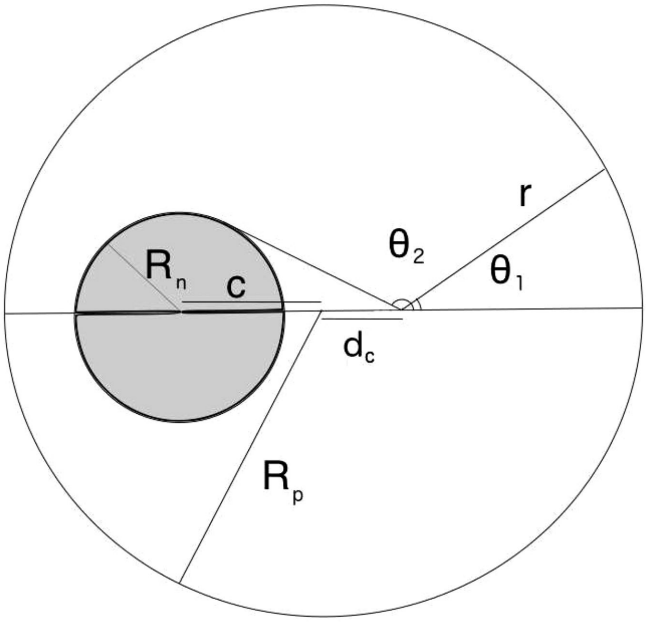

Figure 3. Geometry of crescent sources: the source can be seen as a superposition of a smaller dark disc over and inside a larger brighter disc. R_p and R_n mark the radii of the bright and dark disc. d_c and c mark the distance from the centre of the bright disc to the centroid and from the dark disc to the centroid.

astrophysical sources straddle several caustics, and hence, their net brightness varies smoothly with location. The central engine of quasars, however, is smaller than the typical spacing between caustics. As a result, the lensed brightness undergoes sudden changes as a quasar crosses a caustic. Quasar microlensing is observable at optical wavelengths (e.g. Sluse et al. 2012) and in X-rays (e.g. Neronov, Malyshev & Walter 2016). In principle, it exists at all wavelengths (and has been argued for at cm wavelengths by Koopmans & de Bruyn 2000) but will be washed out if the light is from larger regions than the central engine of the quasar. The effect thus supplies an upper limit on the size of the central engine (e.g. Mediavilla et al. 2015) and can be used to study the mass distribution of stars in the lensing galaxy as well (e.g. Pooley et al. 2012). Microlensing caustics have an additional remarkable feature: though they can be very complicated, they have some universal properties well known from catastrophe theory. In particular, very close to the simplest caustics (known as folds), the magnification is approximately constant on one side and $\propto 1/\sqrt{p}$ where p is the transverse distance of the source from the caustic. This property will be exploited later.

In Section 3 we introduce three source profiles which are used in our subsequent models and simulations: a constant-brightness disc, a circular Gaussian, and the crescent source introduced by Kamruddin & Dexter (2013). The latter is simply a constant-brightness disc with a smaller, non-concentric disc cut out of it. We also derive the half-light radius for a crescent (see Fig. 3). The half-light radius can characterize the source size for all three types of source.

Section 4 shows the light curves that result when each of the model sources crosses an ideal fold. This would apply in Fig. 1 to sources along the path AB or BC, for sources small enough that the curvature of the caustics is negligible. With this assumption one can imagine the caustic as an infinite wall to be crossed by the source as presented in Fig. 2. The source brightness distribution parallel to the caustic naturally makes no difference to the observable brightness; each source can be replaced by an effective one-dimensional source profile, by flattening the source so it becomes perpendicular to the caustic. In principle, the effective one-dimensional brightness profile could be recovered from the light curve by deconvolution. Agol & Krolik (1999) modelled this profile as the result of a circular accretion disc seen through the space–time around a Kerr black hole, and Abolmasov & Shakura (2012) have applied the idea to observed light curves to infer properties of quasar accretion discs. A similar idea appears in Chen et al. (2013). In this work, we take a simpler but arguably more robust approach: we study features in the light curves characteristic of a crescent-like source which in turn would indicate a black hole silhouette. Fig. 4 shows the qualitative features: there is a period during which the dark cutout disc is crossing the caustic, and before and after there are periods when the only the bright parts of the crescent are in transit across the caustic. The details depend on the orientation of the crescent, but basically the dark disc causes a rising light curve to plateau or dip. These features are still present, albeit faintly, if the simple crescent is replaced by a source based on an accretion-disc simulation of a black hole environment (Fig. 9).

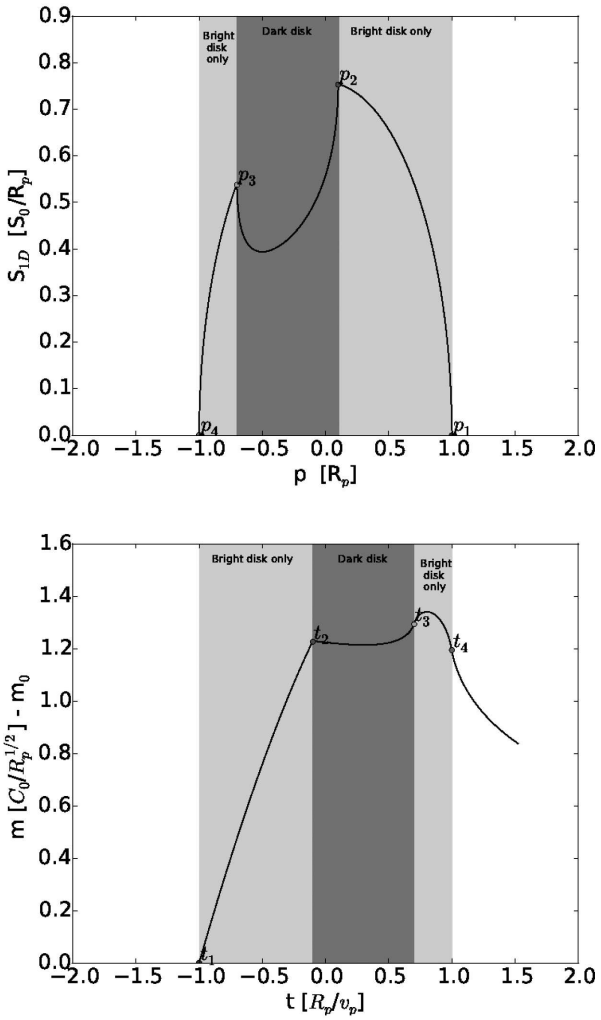

Figure 4. The characteristic points and instances of a crescent source's one-dimensional profile and microlensing light curve. In the top panel a typical 1D profile of a crescent source is presented. There are two light grey regions that mark the regions of the bright disc that are not overlapped by the dark disc. The dark grey band marks the region where the two discs overlap. The points p_1 and p_4 mark the start and end of the bright disc in the 1D representation. Analogously, p_2 and p_3 mark the start and end of the dark disc. The bottom panel represents the associated light curve with the points t_i marking the moment when point p_i overlaps with the caustic. The grey shades are analogous to the ones in the top panel.

In Section 5 we carry out source fitting to light curves, where both noise and systematic errors are present. We generate a mock light curve by taking a crescent source across the path CB in Fig. 1, and then adding noise. The path simulates crossing a clean but not ideal fold. We then fit this light curve to templates from both crescent and circular-Gaussian sources along the paths AB as well as CB. That is, the templates from a similar but not identical caustic are also used, thus deliberately generating a systematic error. Despite this systematic error, a crescent source fits the data, while a Gaussian source is rejected from the χ^2 value.

Finally in Section 6 we discuss in more depth the implications of the results presented in the previously mentioned sections. One of the most interesting implications is the possibility of estimating the black hole mass from the reconstructed parameters. This further requires good approximations of the relative transversal velocity between the quasar and the lens. Proper constraints can be set with independent observations of the stellar structure that contain the gravitational lens.

The thorough study of the possibility to reconstruct the quasar's structural parameters from light curves containing multiple microlensing events represents the target of future work. This will most probably require the use of powerful statistical tools. Another path for future work is the designing of an observation regime best suited for acquiring the necessary microlensed light curve.

2 MICROLENSING

We start by introducing in a succinct manner the gravitational lensing theory that is relevant for microlensing in general and for the scope of the present paper in particular. More detailed presentation of the theory can be found in several references, such as Petters, Levine & Wambsganss (2001).

2.1 Magnification

The gravitational lens equation

$$\vec{\beta} = \vec{\theta} - \vec{\alpha}(\vec{\theta}) \tag{1}$$

relates the apparent sky position $\vec{\theta}$ of a light source to its true but unobservable sky position $\vec{\beta}$ through the bending angle $\vec{\alpha}$. The latter is an integral

$$\vec{\alpha} = (1 + z_{\rm L}) \frac{D_{\rm S} - D_{\rm L}}{D_{\rm S} D_{\rm L}} \frac{4G}{c^2} \int \Sigma(\vec{\theta}') \frac{\vec{\theta} - \vec{\theta}'}{|\vec{\theta} - \vec{\theta}'|^2} \, {\rm d}^2\vec{\theta}' \tag{2}$$

depending on the projected density $\Sigma(\vec{\theta})$ (kg sr^{-1}) of the lens, the lens redshift $z_{\rm L}$ and the comoving distances $D_{\rm L}$ and $D_{\rm S}$ to the lens and source. The derivative of the apparent position with respect to the source position

$$M(\vec{\theta}) = \left(\frac{\partial \beta}{\partial \theta} \right)^{-1} \tag{3}$$

is known as the magnification matrix, and its determinant

$$\mu(\vec{\theta}) = \det |M(\vec{\theta})| \tag{4}$$

is the brightness amplification of an image of a point source. In other words, the source will brighten or dim according to whether $\mu(\vec{\theta})$ is more or less than unity. If there are multiple images at distinct but not observationally resolved $\vec{\theta}_i$ from the same $\vec{\beta}$, a total brightness amplification of

$$\mu_{\rm total} = \sum_i \mu(\vec{\theta}_i) \tag{5}$$

applies. It is possible for the magnification to become formally infinite, as a result of an eigenvalue of the magnification matrix (3) becoming infinite. This generically happens on curves on the $\vec{\theta}$ plane, known as *critical curves*. Mapping a critical curve to the source plane, through the lens equation (1), to the source plane $\vec{\beta}$ gives the so-called caustics. Caustics can appear in the optical system, not just during gravitational lensing. For a point source, caustics are singularities of the magnification; for finite-size sources caustics correspond to high and sharply changing magnification.

Caustics are important in all forms of lensing with multiple images, but they have a special significance for lens quasars, first pointed out by Chang & Refsdal (1979). The granularity of the mass distribution $\Sigma(\vec{\theta})$ due to individual stars produces a caustic network on the scale of $\sqrt{{\rm G M_\odot} D_{\rm L}/c^2}$ or $10^{-6}\sqrt{M/{\rm M_\odot}}$ arcsec for typical lens and source redshift (Wambsganss 2001). Extended sources

wash out this micro-caustic structure, but the optical-continuum and X-ray sources of quasars are even smaller.

2.2 Magnification near a fold caustic

A simple example of a caustic network is shown in Fig. 1. There are two general categories of caustics in gravitational lensing, cusps and fold, and examples of both kinds can be seen in this figure. Magnification near a caustic has universal properties, independent of the system and has been extensively studied (Blandford & Narayan 1986; Schneider & Weiss 1992; Gaudi & Petters 2002a,b). In particular, at distance p from a fold caustic

$$\mu(p) = \mu_0 + C_0 \frac{1}{\sqrt{p}} \Theta(p). \tag{6}$$

Here, the magnification of a point source near a caustic is equal to the sum of the magnification due to other reasons μ_0 (such as zero-point magnification and the effect of other weaker and distant lenses), assumed to be locally constant, and a decrease with the square root of the distance from the fold. The latter term becomes activated only after the source enters the region interior to the caustic curves when the values of the step function $\Theta(p)$ become unity. The proportionality constant C_0 depends on the local conditions in the vicinity of the caustic.

A source of arbitrary shape can be described by a two-dimensional brightness function $S_{2D}(p - p_s, q - q_s)$ defined for a coordinate system p, q where p_s, q_s denote the coordinates of the centre of a source.

For a microlensing event the light curve can be written for an arbitrary source shape as

$$F(t) = \int_{-\infty}^{\infty} \int_{-\infty}^{\infty} S_{2D}(p - p_s(t), q - q_s(t)) \mu_t(p) \mathrm{d}q \mathrm{d}p. \tag{7}$$

In order to build the previous equation we have considered that the time dependence of the flux F is given only by the motion of the source with respect to a fixed caustic. Therefore, the only time dependent quantities in the right-hand side of the equation are the coordinates of the centre of the source $p_s(t)$, $q_s(t)$.

Due to the choice of coordinate system the amplification factor has no dependence on the q coordinate. The previous equation can be rewritten as

$$F(t) = \int_{-\infty}^{\infty} \mu_t(p) S_{1D}\left(p - p_s(t)\right) \mathrm{d}p, \tag{8}$$

where we have defined the one-dimensional flux function as

$$S_{1D}(p - p_s(t)) = \int_{-\infty}^{\infty} S_{2D}(p - p_s(t), q - q_s(t)) \mathrm{d}q. \tag{9}$$

This representation is a valid approximation only when the apparent size of the source is much smaller than the corresponding Einstein angle of the lens. In this context all the information about the source shape and brightness that can be contained in the light curve is exhaustively given by the 1D flux function. In other words, if two sources with different S_{2D} have the same S_{1D} they cannot be distinguished by studying their light curves.

3 MODELS FOR EXTENDED SOURCES

In the present study we analyse three types of sources with different surface brightness:

(1) a rotationally symmetric source with a bivariate Gaussian surface brightness distribution,

(2) a disc source with constant surface brightness distribution,

(3) a crescent-shaped source with constant surface brightness distribution.

The first two sources are the typical choices used in the literature to describe the luminous parts of a quasar. The third one is a recently proposed variant (Kamruddin & Dexter 2013).

3.1 Rotationally symmetric source with a bivariate Gaussian surface brightness distribution

A symmetric 2D Gaussian can be described mathematically as

$$S^{\mathrm{G}}_{2D}(p - p_s, q - q_s) = \frac{S^{\mathrm{G}}_0}{2\pi\sigma^2} \mathrm{e}^{-\frac{(p-p_s)^2}{2\sigma^2}} \mathrm{e}^{-\frac{(q-q_s)^2}{2\sigma^2}}. \tag{10}$$

The corresponding 1D brightness is

$$S^{\mathrm{G}}_{1D}(p - p_s) = \frac{S^{\mathrm{G}}_0}{\sqrt{2\pi}\sigma} \mathrm{e}^{-\frac{(p-p_s)^2}{2\sigma^2}}. \tag{11}$$

Other parameters of the model are the total flux S^{G}_0 and σ.

Although such a definition for a source would have non-zero surface/linear brightness for any coordinate p, q, the amount of light received by a detector from outside a 3σ disc centred at p_s, q_s would be insignificant. For a Gaussian distributed surface brightness source the half-light radius is directly proportional to the parameter σ according to the equation:

$$r_{1/2} = \sqrt{\ln 4}\,\sigma. \tag{12}$$

3.2 Disc source with constant surface brightness distribution

One can construct mathematically a disc source with constant surface brightness and radius R using a step function:

$$S^{D}_{2D}(p - p_s, q - q_s) = \frac{S^{D}_0}{\pi R^2} \Theta\left(R^2 - (p - p_s)^2 - (q - q_s)^2\right). \tag{13}$$

By integrating over q coordinate the linear brightness function is obtained:

$$S^{D}_{1D}(p - p_s) = \frac{2S^{D}_0}{\pi R} \sqrt{1 - \frac{(p - p_s)^2}{R^2}} \Theta\left(R^2 - (p - p_s)^2\right). \tag{14}$$

The half-light radius of a uniform disc source is $R/\sqrt{2}$.

3.3 Crescent source with constant surface brightness distribution

The surface brightness distribution of a geometric crescent can be built by considering two disc sources of constant brightness. One larger disc will contribute positively to the total flux while one smaller disc that is interior to the large one will contribute negatively. This superposition can be written for 2D as

$$S^{C}_{2D} = S^{Dp}_{2D} - S^{Dn}_{2D}, \tag{15}$$

with

$$S^{Dp}_{2D}(p - p_{sn}, q - q_{sn}) = \frac{S^{Dp}_0}{\pi R^2_p} \Theta\left(R^2_p - \left(p - p_{sp}\right)^2 - \left(q - q_{sp}\right)^2\right) \tag{16}$$

and

$$S^{Dn}_{2D}(p - p_{sn}, q - q_{sn}) = \frac{S^{Dn}_0}{\pi R^2_n} \Theta\left(R^2_n - (p - p_{sn})^2 - (q - q_{sn})^2\right) \tag{17}$$

The following notations were used: $R_{\rm p}$ and $(p_{\rm sp}, q_{\rm sp})$ are the radii and coordinate of the centre for the larger positive disc, while $R_{\rm n}$ $(p_{\rm sn}, q_{\rm sn})$ correspond to the smaller negative disc. $S_0^{D\rm p}$, $S_0^{D\rm n}$ represent the total flux of radiation received from the large and small disc. From this point forward we will not use the total flux from each source. Instead, we will use the difference which in this case is the total flux from the crescent-shaped source S_0^C.

Equation (15) can be written as

$$S_{\rm 2D}^C = \frac{S_0^C}{\pi\left(R_{\rm p}^2 - R_{\rm n}^2\right)}\left\{\Theta\left[R_{\rm p}^2 - \left(p - p_{\rm sp}\right)^2 - \left(q - q_{\rm sp}\right)^2\right] - \Theta\left[R_{\rm n}^2 - (p - p_{\rm sn})^2 - (q - q_{\rm sn})^2\right]\right\}. \quad (18)$$

Analogously for the linear brightness function:

$$S_{\rm 1D}^C = \frac{2S_0^C}{\pi\left(R_{\rm p}^2 - R_{\rm n}^2\right)}\left\{\sqrt{R_{\rm p}^2 - (p - p_{\rm sp})^2}\,\Theta\left[R_{\rm p}^2 - \left(p - p_{\rm sp}\right)^2\right] - \sqrt{R_{\rm n}^2 - (p - p_{\rm sn})^2}\,\Theta\left[R_{\rm n}^2 - (p - p_{\rm sn})^2\right]\right\}. \quad (19)$$

There are some constraints on the parameters used to define a crescent in the previously presented manner that need to be stated. First, we must impose the obvious $R_{\rm p} \geq R_{\rm n}$ relation. Secondly, the small disc must always be interior to the large disc:

$$R_{\rm p} \geq R_{\rm n} + \sqrt{\left(p_{\rm sp} - p_{\rm sn}\right)^2 + \left(q_{\rm sp} - q_{\rm sn}\right)^2}. \quad (20)$$

For the distances between the centres of the two discs we will use the same notations as the one found in Kamruddin & Dexter (2013), $a \equiv p_{\rm sn} - p_{\rm sp}$ and $b \equiv q_{\rm sn} - q_{\rm sp}$.

The half-light radius of any source is invariant under any rotational transformation. In the present case of a crescent source the effective radius is dependent on the parameters $R_{\rm p}$, $R_{\rm n}$ and $\sqrt{a^2 + b^2} \equiv c$ exclusively. From symmetry considerations the centroid of the source is collinear with the centres of the two discs and it is situated at a distance d_c from the centre of the bright disc. d_c can be computed numerically with the use of a variation of equation (19):

$$\frac{S_0^C}{2} = \frac{2S_0^C}{\pi\left(R_{\rm p}^2 - R_{\rm n}^2\right)}\int_{d_c}^{R_{\rm p}}\left[\sqrt{R_{\rm p}^2 - p^2} - \sqrt{R_{\rm p}^2 - (p - c)^2}\,\Theta\left(R_{\rm p}^2 - (p - c)^2\right)\right]{\rm d}p. \quad (21)$$

With the position of the centroid determined, the half-light radius can be also be computed through a numerical integral:

$$S_0^C = \frac{4S_0^C}{\pi\left(R_{\rm p}^2 - R_{\rm n}^2\right)}\int_0^{r_{1/2}}[\Theta_2 - \Theta_1]p{\rm d}p,$$
$$\Theta_1 = \left[\pi - \arccos\frac{R_{\rm p}^2 + p^2 - d_c^2}{2R_{\rm p}p} - \arccos\frac{R_{\rm p}^2 - p^2 + d_c^2}{2R_{\rm p}d_c}\right]\Theta(p - R_{\rm p} + d_c),$$
$$\Theta_2 = \pi - \arccos\frac{p^2 + (c + d_c)^2 - R_{\rm n}^2}{2p(c + d_c)}\Theta(p + R_{\rm n} - d_c - c). \quad (22)$$

4 LIGHT CURVES OF THE EXTENDED SOURCES DURING FOLD CROSSING

Using equation (8) and the one-dimensional flux function presented in the previous section one can numerically compute the light curves of the three extended sources for the simplified infinite-wall-caustics model.

4.1 Light curve of the Gaussian source

The amount of light received by an observer from a source with a Gaussian distributed brightness with σ and total flux S_0^G in the absence of any gravitational lensing is

$$F^G(t) = \int_{-\infty}^{\infty}\left(\mu_0 + \frac{C_0}{\sqrt{p}}\Theta(p)\right)\left(\frac{S_0^G}{\sqrt{2\pi}\sigma}{\rm e}^{-\frac{(p - p_{\rm s}(t))^2}{2\sigma^2}}\right){\rm d}p. \quad (23)$$

which can be simplified to

$$F^G(t) = \mu_0 S_0^G + \frac{C_0 S_0^G}{\sqrt{2\pi}\sigma}\int_0^{\infty}\frac{{\rm e}^{-\frac{(p - p_{\rm s}(t))^2}{2\sigma^2}}}{\sqrt{p}}{\rm d}p. \quad (24)$$

4.2 Light curve of the disc-shaped source

Analogous to the Gaussian-shaped source, the disc source with uniform brightness, radius R and unmagnified flux S_0^D has a light curve described by the equation:

$$F^D(t) = \int_{-\infty}^{\infty}\left(\mu_0 + \frac{C_0}{\sqrt{p}}\Theta(p)\right) \times\left[\frac{2S_0^D}{\pi R}\sqrt{1 - \frac{(p - p_{\rm s}(t))^2}{R^2}}\,\Theta\left(R^2 - (p - p_{\rm s}(t))^2\right)\right]{\rm d}p. \quad (25)$$

which is equivalent to

$$F^D(t) = \mu_0 S_0^D + \frac{2C_0 S_0^D}{\pi R} \times\int_{\max(0, p_{\rm s}(t) - R)}^{\max(0, p_{\rm s}(t) + R)}\frac{1}{\sqrt{p}}\sqrt{1 - \frac{(p - p_{\rm s}(t))^2}{R^2}}{\rm d}p. \quad (26)$$

4.3 Light curve of the crescent-shaped source

The light curve of a crescent-shaped source with unamplified flux S_0^C, radii $R_{\rm p}$, $R_{\rm n}$, and centre displacement $a(t)$ is

$$F^c(t) = \mu_0 S_0^C + C_0\frac{2S_0^C}{\pi\left(R_{\rm p}^2 - R_{\rm n}^2\right)} \times\left[\int_{\max(0, p_{\rm s}(t) - R)}^{\max(0, p_{\rm s}(t) + R)}\sqrt{\frac{R_{\rm p}^2 - (p - p_{\rm s}(t))^2}{p}}{\rm d}p - \int_{\max(0, p_{\rm s}(t) - a(t) - R)}^{\max(0, p_{\rm s}(t) - a(t) + R)}\sqrt{\frac{R_{\rm p}^2 - (p - p_{\rm s}(t) + a(t))^2}{p}}{\rm d}p\right]. \quad (27)$$

The function $p_{\rm s}(t)$ can be chosen to be equal to $v_p(t - t_0) + p_{s0}$ where $p_{\rm s0}$ is the coordinate p of the source at the initial time, and v_p is the component of the velocity along the p axis. Such a model of the motion of the object in the source plane describes a linear motion with constant velocity. Furthermore, we reduce the complexity of the model by choosing the function a to be constant in time.

In Fig. 4 there are four characteristic points visible on the resulting one-dimensional light profile of the crescent-shaped source. Two of the points, p_1 and p_4, mark the outer boundaries of the luminous disc component. The other two, p_2 and p_3, mark the boundaries of the dark disc component. Since S_{1D} is a projection of S_{2D} on a line perpendicular to the caustic, the following relation holds:

$$p_2 - p_1 = R_p - R_n - a. \tag{28}$$

In addition, there are two other obvious relations the characteristic points which are independent of the projection:

$$p_4 - p_1 = 2R_p, \tag{29}$$

$$p_3 - p_2 = 2R_n. \tag{30}$$

All four points mark the positions where the derivative $\frac{dS_{1D}}{dp}$ is discontinuous. The points can be used to define three regions: $p_1 - p_2$ where S_{1D} is convex, $p_2 - p_3$ where S_{1D} is concave, and $p_3 - p_4$ where S_{1D} is convex again.

Due to the nature of the caustic and the monotonic behaviour of the magnification map on both sides of the caustic, the previously mentioned characteristic points are inherited by the microlensing light curve. The points on the temporal dimension t_1, t_2, t_3, and t_4 correspond to instances in time when the fold is aligned with p_1, p_2, p_3, and p_4, respectively. For a constant relative velocity v_p between the source and the caustic there is a simple relation between the points p_i and instances t_i:

$$t_j - t_i = \frac{p_j - p_i}{v_p}. \tag{31}$$

With the use of the previous four equations the following identities can be written:

$$R_p = \frac{v_p \times (t_4 - t_1)}{2}, \tag{32}$$

$$R_n = \frac{v_p \times (t_3 - t_2)}{2}, \tag{33}$$

$$a = \frac{v_p \times (t_4 + t_1 - t_3 - t_2)}{2}. \tag{34}$$

Fig. 5 reveals that the light curve of a crescent source has more visible features than the other two light curves corresponding to the disc and Gaussian shape. There are three regions where S_{1D} and by inheritance, the light curve has distinguishable behaviour. The first region that would be recorded on a light-curve plot represents the period of time when the bright disc begins to be overlapped by the caustic and stops when just before the dark disc reaches the caustic. During this period of time, the flux of light from the source is increasingly magnified. The second period starts and ends with the overlapping of the dark disc. As a boundary of the two regions, there is a distinguishable point where the slope of the magnification is drastically changed. This apparent discontinuity in the first derivative of the magnification function is caused by the caustic amplification of the sudden drop in the S_{1D} function. During the respective period, the magnification growth slows or even reverses and later starts to grow faster again as the dark disc ends its overlap with the caustic. At the point where the dark disc clears the caustic, the growth of the magnification is infinite, which appears as a saddle point on the light curve. Next, the final period corresponds to the case when the dark disc has cleared the caustic and the bright disc continues to overlap with the caustic. During this period, the light curve reaches a peak that for most of the parameter space is global and for the rest of the parameter space local. At

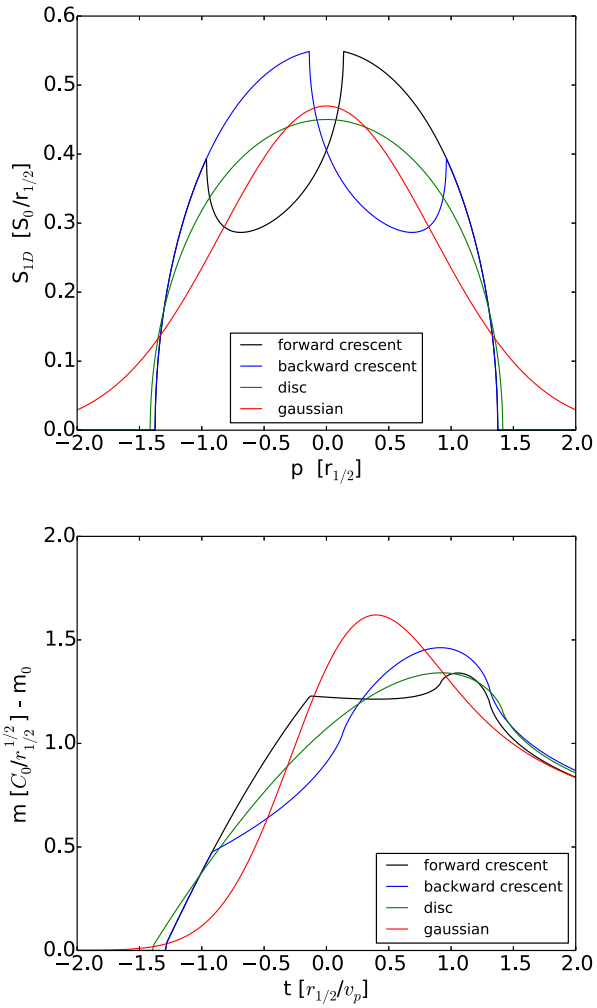

Figure 5. 1D profiles (top panel) and simulated light curves (bottom) of crescent, Gaussian, and disc sources with identical total flux (S_0) and half-light radius ($r_{1/2}$). Crescent source has $r_{1/2} = 0.72754\ R_p$, $R_n = 0.4\ R_p$, $a = 0.3/-0.3\ R_p$.

the end of the period, the growth of the magnification is negative infinite. The respective point appears as a second saddle point on the light curve. Past this point the magnification of any finite source will decay in roughly the same manner.

The impact of parameter a on the shape of the light curve can be observed in Fig. 6. Sources where the centre of the dark disc reaches the caustic before the centre of the bright disc are characterized by a smoother broad peak in contrast to the cases where the centre of the dark disc reaches the caustic after the bright disc. In the case of the latter the instance when the dark disc reaches the caustic corresponds to larger and larger magnifications until it becomes a local and even global peak. The effect of the R_n parameter on the light curve is presented in Figs 7 and 8. For the particular set of parameters where $R_p = R_n + a$ the third period of time discussed previously does not exist. Particularizing further, if the value of the radius of the dark disc is comparable to the value of the radius of the bright one then the position and shape of the maximum magnification are strikingly different. In case the crescent reaches the caustic with the bright region first, the peak magnification happens when the dark region reaches the caustic and it is characterized by a sharp variation in magnification growth. In the opposite case, the peak appears before

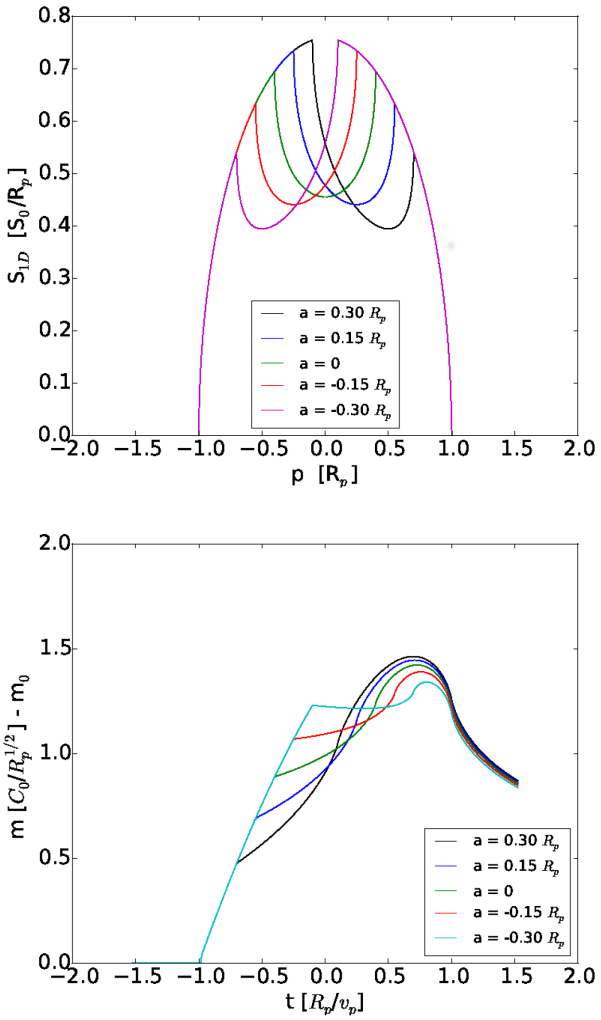

Figure 6. 1D profiles (top panel) and simulated light curves (bottom) of crescent sources with identical R_p and R_n ($R_n = 0.4\ R_p$) and different disc centres displacement (a).

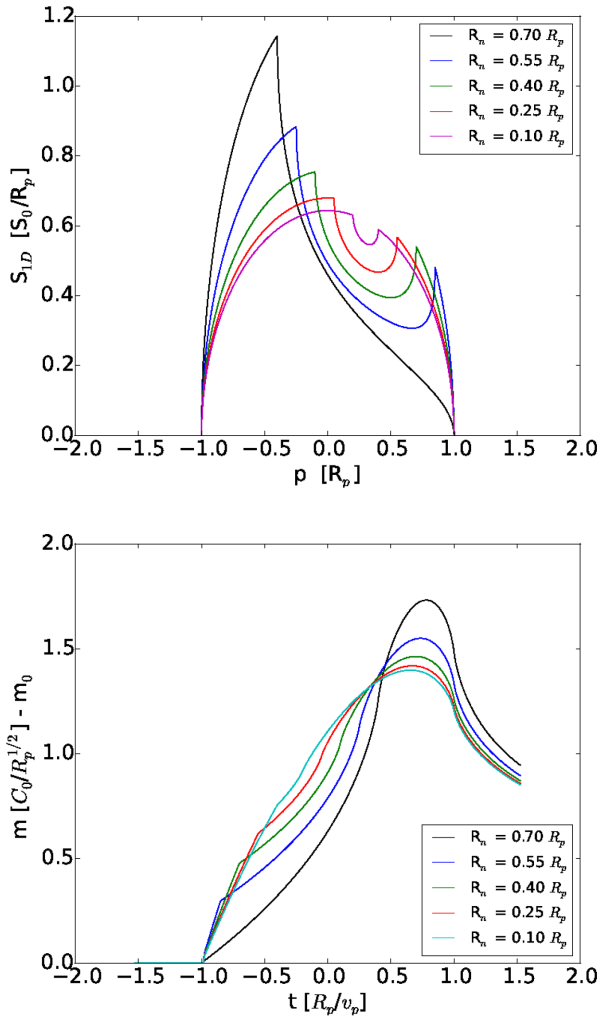

Figure 7. 1D profiles (top panel) and simulated light curves (bottom) of backwards crescent sources with identical R_p and a ($a = 0.3\ R_p$) and different dark disc radii (R_n).

the end of the bright disc reaches the caustic and the shape of the light curve is smoother.

4.4 Microlensing a simulated image of M87

Dexter, McKinney & Agol (2012) have created a radiative image of M87 based on the GRMHD simulations presented in (McKinney & Blandford 2009). The top right-most image in fig. 5 of Dexter et al. (2012) has been projected to a 1D profile associated with the perpendicular direction to a fold caustic approaching the image from the right. The projection is presented in the upper panel of Fig. 9. The amplification values of the flux of light corresponding to a microlensing event are presented in the lower panel of Fig. 9. In general, the behaviour of the light curve is similar to the geometric crescent source with the caveat that the outer regions surrounding the luminous parts of the image have non-zero flux and thus are more extended than the simplified source model.

5 FITTING MOCK DATA

Having used the simple model of an ideal fold to gain insight, we now consider the question of whether the characteristics of a crescent source could be discerned in real data having noise and systematic error as well. To do so, we first generate a microlensing light curve using a widely used microlensing code (Wambsganss 1990, 1999; Wambsganss et al. 1999) to which we have added a small extension to provide the option of crescent sources. We then fit model or template light curves – which are generated with varied source and other parameters – to the mock light curve. The basic technique is the same as in previous studies (e.g. Poindexter & Kochanek 2010) though the details are different.

5.1 Numerical microlensing light curves

The microlensing code uses a ray-shooting technique to compute the gravitational lensing effect of a mass distribution consisting of (a) a smooth component and (b) a random distribution of point masses representing stars. The ray shooting maps a grid of $\vec{\theta}$ to $\vec{\beta}$ using the lens equation (1). That is, the rays are shot from the observer back to the source. For the computation of the individual deflection angles $\vec{\alpha}(\vec{\theta})$ a hierarchical or tree method is used. The positions of all lensing masses are put into a grid of $\vec{\theta}$. Each grid cell is subdivided into four smaller squares recursively until every cell contains only one mass. Nearby masses are added individually while distance

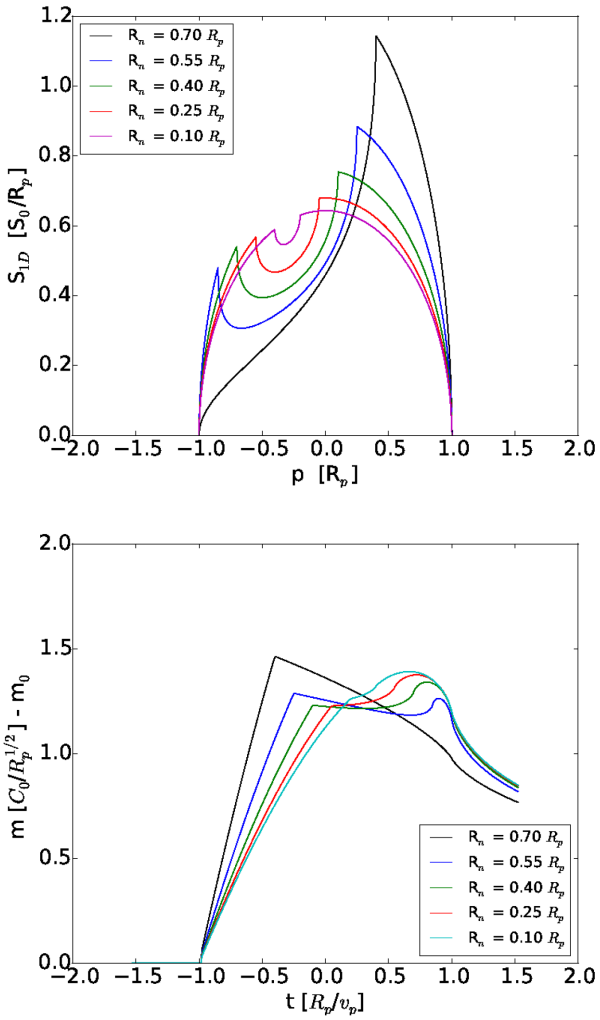

Figure 8. 1D profiles (top panel) and simulated light curves (bottom) of forwards crescent sources with identical $R_{\rm p}$ and a ($a = -0.3\,R_{\rm p}$) and different dark disc radii ($R_{\rm n}$).

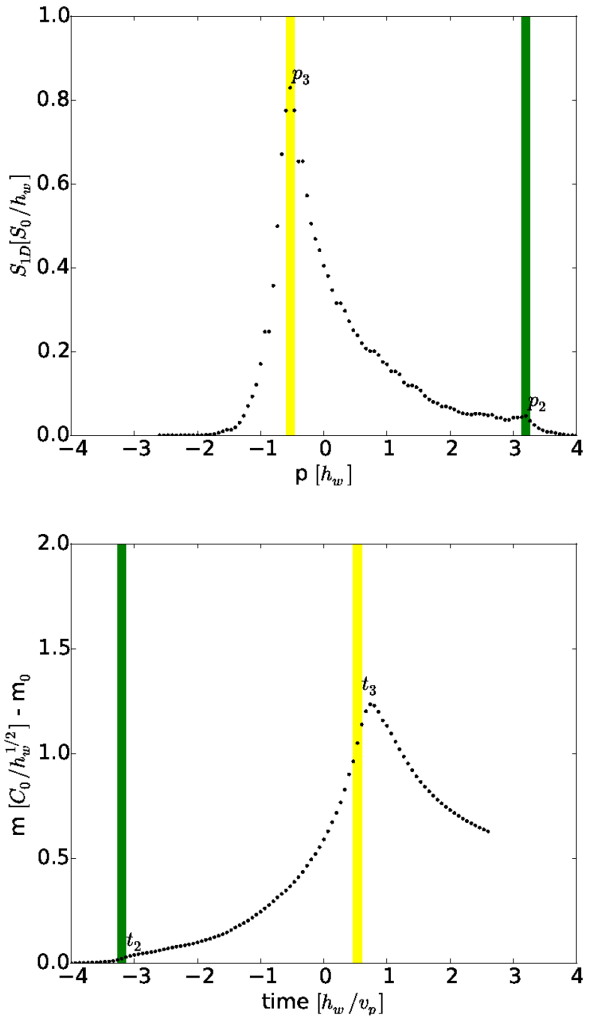

Figure 9. The one-dimensional profile obtained from the numerical integration along the ordinate axis of a simulated source image is presented in the upper panel. The source image was presented in Dexter et al (2012) in the top right-most panel of Fig. 5 (of the respective paper) as a result of the simulations presented in McKinney & Blandford (2009). The corresponding light curve associated with the 1D profile is presented in the lower panel. The points p_2 and p_3 mark the start and end of the equivalent dark disc and are associated with the moments of their overlap with the caustic: t_2 and t_3; $h_{\rm w}$ denotes the maximum width of the crescent.

masses are clumped into larger grid cells whose net contribution is approximated by its first few multipole moments. Scaled units are used, with the constant pre-factor in the deflection angle (2) separated out. The result of ray shooting is a pixel map on the $\vec{\beta}$ plane of the number of lightrays which arrive at the source plane from a particular observer. This intermediate result is effectively a magnification map on the source plane.

When generating the magnification map depicted in Fig. 1, which is used in our analysis below, only two point masses were included. This was done in order to have clean fold caustics. There was no smooth component.

Once the map is created, the light curve can be obtained by specifying the transit path of the source across the map. The source is moved along the transit line, one pixel at a time, and at each step the brightness distribution of the source is convolved (equation 7) with the magnification map to give the observable total brightness. In real life, not only are both lens and source moving but the lens configuration, and with it the magnification pattern, is also changing with time. The first subtlety is taken care of by a coordinate transformation in this analysis; the second one is not considered, and the lens configuration is assumed to be constant in time.

For the purpose of this analysis, it is desirable to mimic the analytical behaviour of a simple fold as much as possible. Accordingly, we generated a mock light curve by taking a crescent source along the path CB in Fig. 1. The crescent parameters (as defined in Section 3.3) were

$$\left(R_{\rm p}, \frac{R_{\rm n}}{R_{\rm p}}, \frac{a}{R_{\rm p}}, \frac{b}{R_{\rm p}}\right) = (1.31, 0.4, 0, 0.3) \qquad (35)$$

corresponding to $r_{1/2} = 1$. Unit length has 30 pixels on the magnification map. The source was carried for 250 pixels along the path CB, giving 251 brightness values. Gaussian noise at 4 per cent of the current brightness was then added to give the mock data.

The time unit for the light curve is taken to be $r_{1/2}/v_p$ where v_p is the velocity transverse to the caustic. If we assume the brightness measurements are nightly, and $v_p = 200\,{\rm km\,s^{-1}}$, the length of the microlensing event (250 d) is comparable to typical observed events (see e.g. Mediavilla et al. 2015). The implied $r_{1/2}$ is $\sim 10^{14}$ cm, which

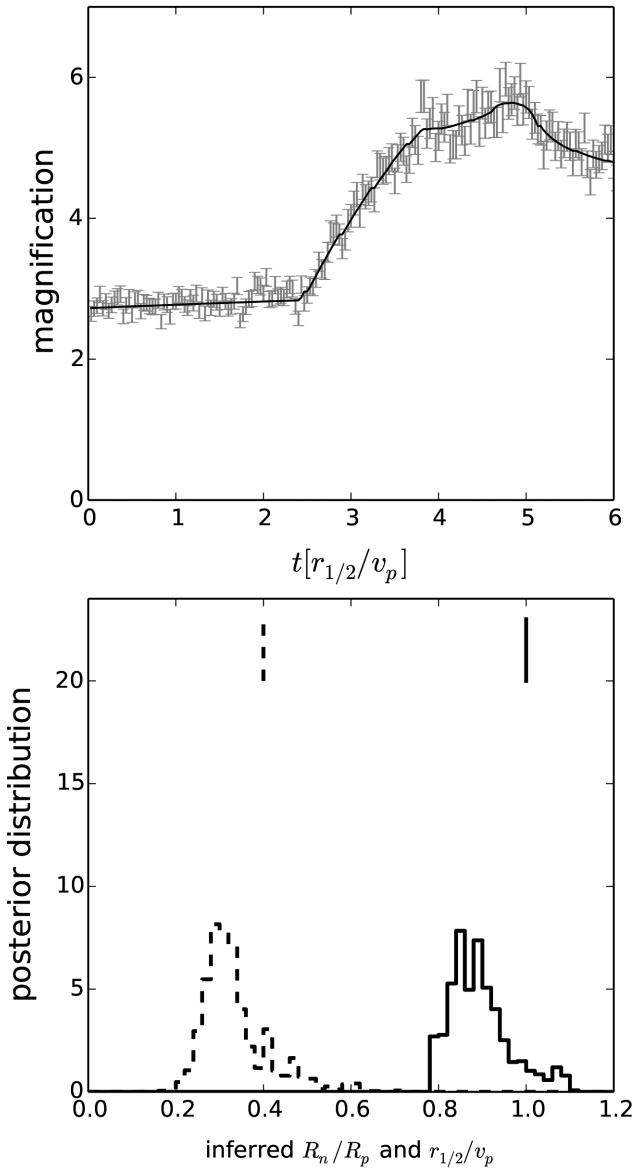

Figure 10. Mock light curve fitted with the correct source type and caustic. The upper panel shows the mock data points, and running through them is a seven-parameter best fit: these being the crescent parameters (R_p, R_n, a, b) and additionally the start and end times and the overall normalization. (Ideal light curves for the same crescent parameters appear above in Figs 4–6 and 8.) The curve has $\chi^2_{(244)} = 243$, $P = 0.32$ indicating a good fit. (The subscript 244 refers to degrees of freedom: 251 points less 7 parameters.) The lower panel shows the posterior distributions for $r_{1/2}/v_p$ (solid histogram) and $R_\mathrm{n}/R_\mathrm{p}$ (dashed histogram). Vertical dashes mark the correct values. Inferred are $r_{1/2}/v_p = 0.90^{+0.15}_{-0.07}$ and $R_\mathrm{n}/R_\mathrm{p} = 0.32^{+0.19}_{-0.08}$ (90 per cent confidence).

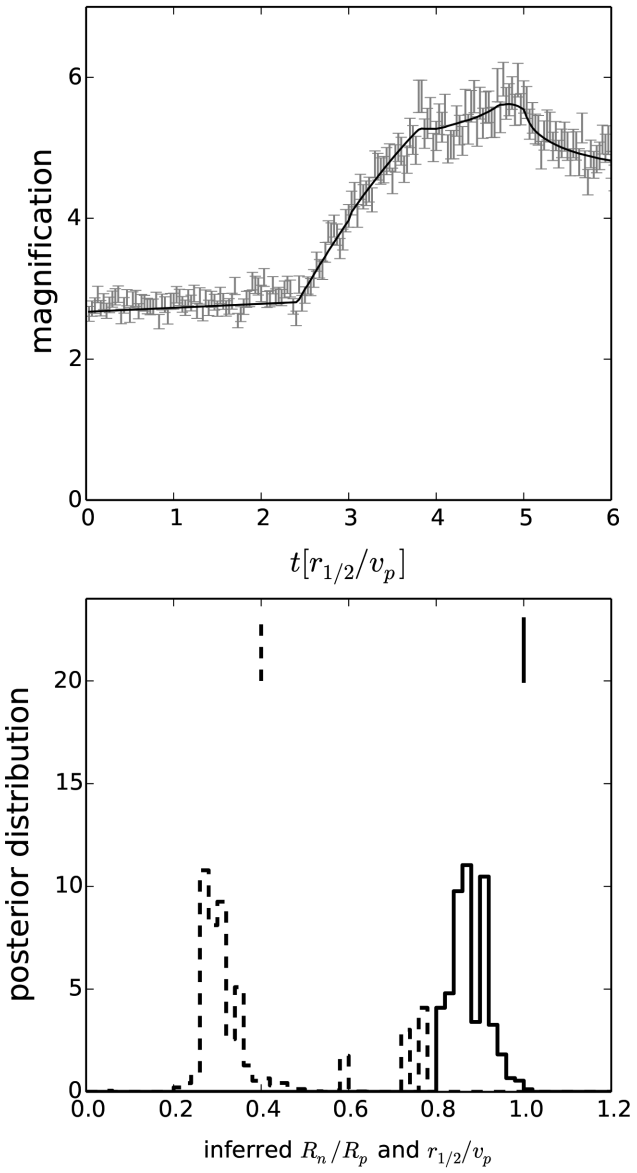

Figure 11. Like Fig. 10, except that the fit is derived from a slightly different caustic than the one used to generate the mock data. The curve has $\chi^2_{(244)} = 284$, $P = 0.01$ indicating a marginally acceptable fit. Inferred are $r_{1/2}/v_p = 0.92^{+0.06}_{-0.04}$ and $R_\mathrm{n}/R_\mathrm{p} = 0.32^{+0.12}_{-0.07}$ (90 per cent confidence).

is at the lower end of values inferred for microlensed X-ray sources, whereas for optical sources, the inferred $r_{1/2}$ is one to two order of magnitude larger (see e.g. fig. 8 of Mosquera et al. 2013).

The mock data appear in Figs 10–12. Illustrative values have been adopted for the frequency of observations and for the noise level. It is, of course, important that the observations have enough sampling and signal to noise that the characteristic features of a crescent source (see e.g. Fig. 4) are not washed out.

5.2 Model-fitting results

We now proceed to fit the mock light curve. MCMC is used to fit source parameters and additional nuisance parameters (see below) jointly, and then marginalize out all uninteresting parameters, leaving posterior distributions for any chosen parameter.

In addition to the source parameters, the fitting procedure includes three nuisance parameters, namely the brightness normalization and the start and end points on the path. The latter two are equivalent to considering the location of the caustic with respect to the starting point and the velocity component of the source transverse to the caustic (that is, v_p). The orientation of the source track is another nuisance parameter. For an ideal fold, changing the orientation of the source track is equivalent to changing v_p and the orientation of the source (see Fig. 2). Since the latter two parameters are accounted for, we do not include the orientation of the track as a separate

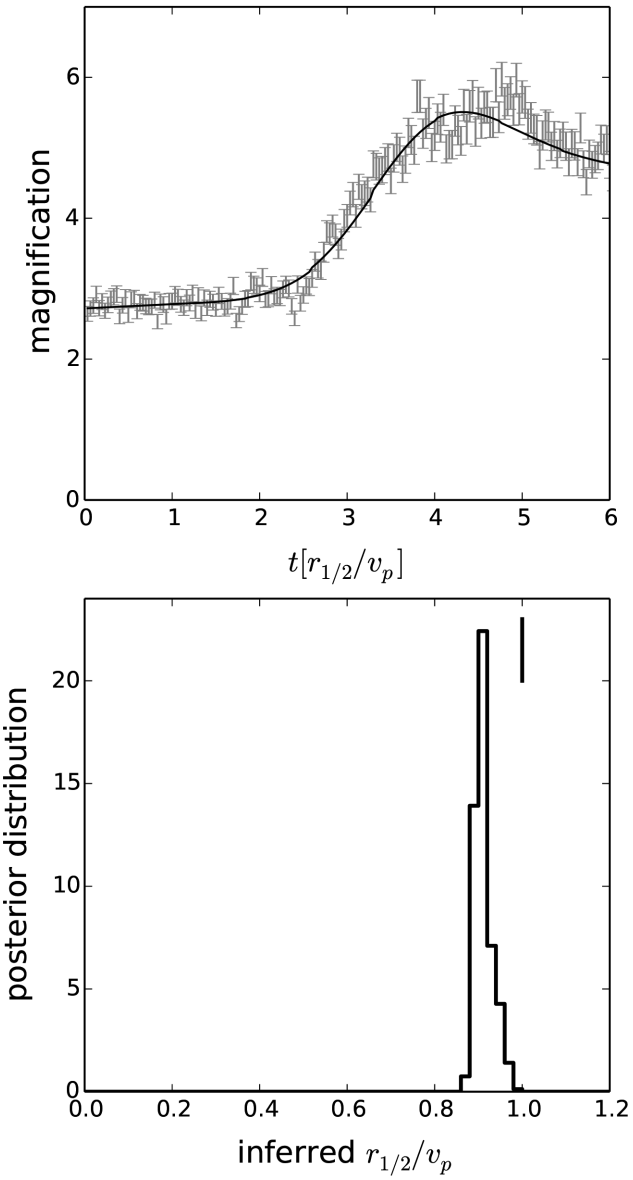

Figure 12. Like Figs 10 and 11, but showing the best fit to a Gaussian source. The histogram shows the posterior distribution of $r_{1/2}/v_p$ (there is no R_n). It appears to show $r_{1/2}/v_p$ as accurately recovered, but is not to be trusted, because the fit has $\chi^2_{(247)} = 344$, $P = 3 \times 10^{-6}$ indicating rejection of the Gaussian source. Looking closely, the curve is a little too shallow near $t = 3$, and it is unable to fit the second sub-peak near $t = 5$. Inferred is $r_{1/2}/v_p = 0.91^{+0.05}_{-0.01}$ (90 per cent confidence).

parameter. Since the caustic is not an ideal fold, disregarding the orientation of the source track can be expected to introduce some systematic error.

Figs 10–12 show the numerical results. Each of these figures shows the mock data (the same in all three cases) along with best fits and the fitted values and uncertainties on $r_{1/2}/v_p$ and (if applicable) R_n/R_p.

Fig. 10 shows a test of the fitting procedure. The computer compares the mock data to different template light curves. The templates come from taking a crescent source along the path CB in Fig. 1, but with varied crescent parameters and varied start and finish points. As the figure shows, the light curve can be fitted to within the noise, and the parameters $r_{1/2}/v_p$ and R_n/R_p can be recovered.

Fig. 11 attempts a somewhat more realistic situation. The mock light curve is the same as before, but the templates come from taking a crescent source along the path AB in Fig. 1. That is, the mock data and the templates come from crossings of different caustics. This is intended to mimic the systematic errors arising from not knowing the caustic exactly. As Fig. 11 shows, the fit is slightly degraded, but still acceptable. The parameters $r_{1/2}/v_p$ and R_n/R_p are still recovered, though less well; the correct value of $r_{1/2}/v_p$ lies outside 90 per cent of the MCMC distribution, but within 99 per cent. The parameters a/R_p and b/R_p (not shown in the figure) giving the orientation of the crescent were not correctly recovered; but this expected, because the AB and CB tracks have different orientations with respect to the caustics crossed. The slight degradation of the fit can be understood as follows. The source track will not, in general, be normal to the caustic, but will instead have a non-normal velocity component. If the caustic is perfectly straight, the velocity component along the caustic makes no difference. (Hence our model only considers only the normal velocity component v_p). But in fact the caustics, although clean folds do have some curvature. The combination of a curving caustic and non-normal velocity of the source makes the orientation of the source twist with respect to the caustic. This twist would be different for crossings along the AB and CB tracks.

Fig. 12 shows the result of attempting to fit templates from a Gaussian source to the same mock data. There is a small but statistically very significant misfit because a Gaussian source cannot reproduce the part of the light curve with the slight flattening and then a second sub-peak (cf. Fig. 4) as the dark part of the crescent crosses the caustic. A hint of such a feature is present in recent caustic-crossing observations of the well-known system Q2237+0305 (see fig. 3 in Mediavilla et al. 2015) though interpretation as a crescent source is speculation at present.

6 DISCUSSION

In the current paper, we simulate and study the resulting microlensing light curves of geometric crescent-shaped sources and compare them with the microlensing light curves of other simple mathematically describable source profiles. In order to mimic the behaviour of the flux of light from the source in the proximity of a fold caustic, we make use of the simple approximation described in equation (5). The equation would exhaustively describe the magnification map and offer a good universal approximation for the particular microlensing regime that we consider. Namely, the shape of the caustic boundary in the proximity of the source in the respective plane can be approximated by a line due to reason that the local radius of curvature of the caustic is orders of magnitude greater than the half-light radius of the studied source.

The first two source profiles that we consider are the uniform disc and the symmetric Gaussian source. Both of them can be described by a half-light radius ($r_{1/2}$) and a total unlensed light flux (S_0). With the two parameters constrained the one-dimensional profiles, as well as the light curves of the two source, are completely determined, since no free parameter remains.

The previous statement does not hold for a crescent source. In the case of the crescent source there are in total five parameters: the integrated flux of the source S_0, the radii of the bright and dark discs and the displacement of the centres of the two discs on the axes perpendicular and parallel to the caustic.

Since the one-dimensional source profile that corresponds to an axis perpendicular to the caustic contains exhaustively all the information regarding the source that can be revealed by the light curve, the value of the crescent's discs centres displacement parallel to the caustic does not have an effect on the shape of the light curve.

Nevertheless, the respective displacement is relevant for the calculation of the half-light radius. Its qualitative effect is to decrease the value of the half-light radius when the absolute value of the parameter is increased. In contrast to the simpler source shapes discussed before the crescent has two additional relevant parameters: the radius of the dark disc (R_n) and the centre displacement in the direction perpendicular to the caustic a.

Fig. 5 reveals that the light curve of a crescent source has more visible features than the other two light curves corresponding to the disc and Gaussian shape. The parameters R_n and a have strong influences on the shape of the microlensed light curve as can be seen in Figs 6–8. Moreover, the one-dimensional source profile corresponding to the direction perpendicular to the caustic reveal four characteristic points. The overlap of each of these points with the caustic leaves visible features on the light curve at the corresponding instances of time. In time order, the instances correspond to the start of the overlap between the caustic and the bright disc, the start of the overlap between the caustic and the dark disc, the end of the overlap between the caustic and dark disc and finally the end of the overlap between the caustic and the bright disc.

With the different source profiles and their corresponding light curves studied we can change our point of view of the system to that of an observer. The observer would basically detect only the light curve of such a source. As described in Section 4.3 the timing of the onset and offset of the previously described periods can be used to estimate the values of the radii and one of the displacement parameters when assuming a geometric crescent. All quantities can be estimated in terms of the relative velocity of the source in a direction perpendicular to the caustic.

Furthermore, a simulated image of M87 presented in Dexter et al. (2012) has been microlensed (Fig. 9). On the resulting light curve the instances corresponding to the start and end of the black hole shadow and caustic overlap were distinguishable.

In the case of a high-quality light curve, provided the caustic is a fairly clean fold, or equivalently, the source is much smaller than the local radius of curvature of the caustic, the crossing times of the bright and dark areas (cf. Fig. 4) could be estimated by simply identifying signatures on the light curve corresponding to transits of the particular source features across the caustic. This simple idea can be supplemented with statistics. In Section 5, we take a realistic magnification map generated by the microlensing code from Wambsganss et al. (1999), compute a caustic-crossing light curve from it, and then fit the light curve with other caustic-crossing templates. The conclusion is that a crescent source can be distinguished from a circular source, on the basis of caustic-crossing light curves, if the caustic is a clean but not ideal fold.

The previously mentioned abstract parameters can be related to physical quantities specific to the central region of a quasar. As such the luminous region would correspond to the bright accretion disc that surrounds the black hole. The later's gravity would cause a shadow in the bright region limited by the extent of the event horizon of the black hole. Therefore, the radius of the bright disc would provide an estimate of the size of the accretion disc and the radius of the dark disc would provide and estimate of the gravitationally magnified Schwarzschild radius of the black hole $R_S^{\text{magnified}} = \Delta t_{\text{dark}} v_p$. By $R_S^{\text{magnified}}$ we refer to the apparent Schwarzschild radius which is larger than the real value at large distances due to the black hole's own gravity. Moreover, the gravitationally magnified value of the Schwarzschild radius is a monotonic function of the black hole's mass. Therefore, it can be used to estimate the mass of the black hole if it was not rotating. In the previous expression, the Δt_{dark} denotes the period of overlap between the black hole shadow and fold caustic, while v_p denotes the component of the relative velocity of the source and fold which is perpendicular to the caustic.

The parameters whose values cannot be determined due to the loss of information from the directions parallel to the caustic could be obtained in the eventuality in which the same source crosses multiple caustics that are not parallel. Multiple crossing of caustics can reveal details of the one-dimensional flux profile corresponding to multiple distinct directions which would allow the reconstruction of the two-dimensional profile analogous to the process through which an image of a CT scan is obtained.

ACKNOWLEDGEMENTS

IM is supported by Fermi Research Alliance, LLC under Contract No. De-AC02-07CH11359 with the United States Department of Energy. JW would like to acknowledge and thank the Pauli Center for Theoretical Studies of ETH Zurich and University of Zurich for generous support during the Schrödinger visiting professorship in 2013.

Author contributions. Prasenjit Saha provided the original idea and plan for the research project as well as multiple contributions to the analysis and manuscript preparation. Mihai Tomozeiu simulated and studied the ideal behaviour of the microlensing light curves for the different source profiles discussed and prepared the manuscript. Joachim Wambsganss contributed to the research planning and provided the numerical code used by Manuel Rabold to create the magnification map and corresponding light curves used in the MCMC analysis performed by Irshad Mohammed in the last part of the presented work. Both Manuel Rabold and Irshad Mohammed had large contributions in writing the 'Fitting Mock Data' section.

REFERENCES

Abolmasov P., Shakura N. I., 2012, MNRAS, 423, 676
Agol E., Krolik J., 1999, ApJ, 524, 49
Begelman M. C., Blandford R. D., Rees M. J., 1984, Rev. Mod. Phys., 56, 255
Blandford R., Narayan R., 1986, ApJ, 310, 568
Broderick A. E., Fish V. L., Doeleman S. S., Loeb A., 2011, ApJ, 738, 38
Chang K., Refsdal S., 1979, Nature, 282, 561
Chen B., Dai X., Baron E., Kantowski R., 2013, ApJ, 769, 131
Dexter J., Agol E., Fragile P. C., McKinney J. C., 2010, ApJ, 717, 1092
Dexter J., McKinney J. C., Agol E., 2012, MNRAS, 421, 1517
Doeleman S., 2008, J. Phys. Conf. Ser., 131, 012055
Doeleman S. S. et al., 2008, Nature, 455, 78
Doeleman S. S. et al., 2012, Science, 338, 355
Fish V. L. et al., 2016, ApJ, 820, 90
Gaudi B. S., Petters A. O., 2002a, ApJ, 574, 970
Gaudi B. S., Petters A. O., 2002b, ApJ, 580, 468
Kamruddin A. B., Dexter J., 2013, MNRAS, 434, 765
Koopmans L. V. E., de Bruyn A. G., 2000, A&A, 358, 793
Lynden-Bell D., 1969, Nature, 223, 690
McKinney J. C., Blandford R. D., 2009, MNRAS, 394, L126
Mediavilla E., Jiménez-vicente J., Muñoz J. A., Mediavilla T., 2015, ApJ, 814, L26
Mościbrodzka M., Gammie C. F., Dolence J. C., Shiokawa H., Leung P. K., 2009, ApJ, 706, 497

Mosquera A. M., Kochanek C. S., Chen B., Dai X., Blackburne J. A., Chartas G., 2013, ApJ, 769, 53
Neronov A., Malyshev D., Walter R., 2016, preprint (arXiv:1602.07601)
Pâris I. et al., 2014, A&A, 563, A54
Petters A. O., Levine H., Wambsganss J., 2001, Singularity Theory and Gravitational Lensing, Birkhäuser, Boston
Poindexter S., Kochanek C. S., 2010, ApJ, 712, 658
Pooley D., Rappaport S., Blackburne J. A., Schechter P. L., Wambsganss J., 2012, ApJ, 744, 111
Salpeter E. E., 1964, ApJ, 140, 796
Schneider P., Weiss A., 1992, A&A, 260, 1
Sluse D., Hutsemékers D., Courbin F., Meylan G., Wambsganss J., 2012, A&A, 544, A62
Wambsganss J., 1990, PhD thesis, Ludwig-Maximilians-Univ., Munich, Germany
Wambsganss J., 1999, J. Comput. Appl. Math., 109, 353
Wambsganss J., 2001, PASA, 18, 207
Wambsganss J., Brunner H., Schindler S., Falco E., 1999, A&A, 346, L5
Zel'dovich Y. B., Novikov I. D., 1964, Sov. Phys. Dokl., 9, 246

This paper has been typeset from a TEX/LATEX file prepared by the author.